

# The ultimate bearing capacity of rectangular tunnel lining assembled by composite segments: An experimental investigation

Xian Liu<sup>1a</sup>, Xinyu Hu<sup>\*2</sup>, Linxing Guan<sup>3</sup> and Wei Sun<sup>3</sup>

<sup>1</sup> College of Civil Engineering, Tongji University, 1239 Siping Road, Shanghai, China

<sup>2</sup> College of Urban Construction and Safety Engineering, Shanghai Institute of Technology, 100 Haiquan Road, Shanghai, China

<sup>3</sup> Shanghai Municipal Engineering Design Institute (Group) Co. Ltd., 901 North Zhongshan no.2 Road, Shanghai, China

(Received August 03, 2016, Revised April 05, 2017, Accepted May 02, 2017)

**Abstract.** In this paper, full-scale loading tests were performed on a rectangular segmental tunnel lining, which was assembled by steel composite segments, to investigate its load-bearing structural behavior and failure mechanism. The tests were also used to confirm the composite effect by adding concrete inside to satisfy the required performance under severe loading conditions. The design of the tested rectangular segmental lining and the loading scheme are also described to better understand the bearing capacity of this composite lining structure. It is found that the structural ultimate bearing capacity is governed by the bond capacity between steel plates and the tunnel segment. The failure of the strengthened lining is the consequence of local failure of the bond at waist joints. This led to a fast decrease of the overall stiffness and eventually a loss of the structural integrity.

**Keywords:** rectangular tunnel lining; composite segment; full-scale test; failure mechanism; ultimate bearing capacity

## 1. Introduction

It is well known that shield driven tunnels of rectangular cross-section have several advantages including the fact that underground space can be more effectively utilized, with the configuration of the tunnel matches the purpose of the tunnel, and the cover depth and the corresponding quantity of excavation reduced as a result of the absence of soil-arching effect. Nonetheless, rectangular tunnels of regular RC structure are more difficult to construct and do not provide the same level of stability which is characterized by the uneven distribution of internal force around the whole lining structure (not having a center pillar), i.e., the maximum positive and negative bending moment develop at the middle of the longer side and the shorter side respectively, and the higher shear forces exist at the corner of both the top and bottom part. Therefore, to address the aforementioned problem, the sandwich type composite structure which is originally proposed by Tomlinson (Tomlinson *et al.* 1989) is well introduced in rectangular segmental tunnel engineering. In this structure (known as steel-concrete-steel segments, SCS), the segments have stud shear connectors on full steel skin plates which produce the composite effect by acting together with the concrete inside. Joints are such that joint plates are tightened by bolts.

SCS composite structure has a vast range of applications in many domains, such as bridge engineering, protective structures, offshore structures, etc. Previous research on this technique has been conducted focusing mainly on the

performance of the composite beam elements, slabs or panels in structure engineering (Subedi and Coyle 2002, McKinley and Boswell 2002, Clubley *et al.* 2003, Liang *et al.* 2004, Xie *et al.* 2007, Dai and Liew 2010, Yang *et al.* 2016). In addition, numerical and experimental methods were also adopted to study the failure mechanism of these composite structures (Johnson and David 2010, Leveque *et al.* 2013, Tian *et al.* 2014, Zou *et al.* 2016). Based on these investigations, it was concluded that SCS composite structure can improve the ultimate load-bearing capacity with its advantages of light weight, high strength and superior ductility. In shield tunnel engineering, SCS composite segments have been successfully employed in the project of Kyoto Subway Tozai Line in Japan in 2003, which was the world's first shield driven subway tunnel of rectangular shape. Before the full application, full-scale loading tests were performed to confirm the adequacy of the design (Nakamura *et al.* 2003). However, due to the unique characteristics of the underground structure, the mechanical behavior of SCS composite structural elements like beams and panels cannot be directly used in shield tunnel linings (i.e., segmental rings), which consist of segments and many connecting joints and thus show complicated mechanical behavior under different combined loads. As a result, in 2009, Zhang Wenjun developed a mechanical model which can be used to analyze the nonlinear behavior of composite segment with discrete partial connection under combined loads. The work by Zhang (2009) serves as a fundamental contribution to better understand and model the behavior of the composite structure of circular tunnel lining. However, for SCS composite structure with specific rectangular segmental tunnel lining, no research on its bearing performance or any corresponding rational design method have been published so far.

\*Corresponding author, Ph.D., Associate Professor,  
E-mail: [christiehxy@163.com](mailto:christiehxy@163.com)

<sup>a</sup> Ph.D., Associate Professor, E-mail: [xian.liu@tongji.edu.cn](mailto:xian.liu@tongji.edu.cn)

Since it is hard to predict precisely the ultimate bearing capacity of the composite segments lining by conventional structural analysis, a full-scale experimental method for rectangular tunnel lining is required to identify its mechanical behavior and the structural performance. This includes the investigation of different failure modes in terms of the overall deformation and consequent force distribution, which have shown to be an effective way to understand the structural bearing capacity. Besides, it is a crucial to investigate the nonlinear force distribution and displacement variation of longitudinal joints which can be directly used to verify the sealing and waterproof performance in composite segments lining. Therefore, the main purpose of this research was to investigate the ultimate bearing capacity of rectangular segmental lining with SCS composite structure. For this purpose, the paper is organized as follows: full-scale tests on rectangular tunnel lining, strengthened by means of steel plates, will be introduced (as shown in Fig. 1(a)). Special attention will be paid to the developed measurement system concerning loading and deformations. Then, the failure process will be described in detail and the main experimental results of the full-scale tests will be presented. Finally, the failure mechanism and the ultimate bearing capacity of SCS composite tunnel lining will be investigated and discussed.

**2. Experimental program**

The steel-concrete filled closed-composite segments formed the lining structure and were designed, manufactured and air-cured before the tests, with critical steps including welding steel plate, fixing steel bars and casting concrete. In SCS composite structure, shear connector which helps to tie together steel element and concrete element at an interface is crucial to the composite

action. Shear stud connector, is one of the common type of the mechanical shear connector used, consisting of a bolt which is welded to the steel element. In such cases, the studs must be designed at the reasonable intervals to resist the longitudinal shear forces at the steel-concrete interface, as well as to effectively prevent separation between the steel and concrete in order to guarantee the same curvature of the two elements. Taking semi-structure of segment F, the details of the connectors in the lining structure are illustrated in Figs. 1(b) and (c), there are two lines of studs along 550 mm's lining thickness, with the interval of 200 mm in each curved line which is parallel with central axial; while in longitudinal direction, the studs are mounted every 200 mm's distance. For each stud, the diameter is 16 mm, an the total height is 90 mm.

**2.1 Experimental specimen**

Full-scale loading tests were performed on SCS composite tunnel lining segments to confirm the adequacy of the design. As shown in Fig. 1(a), the outside diameter of the lining is 9750 mm and 4950 mm, respectively, the thickness of the lining is 550 mm. The lining consists of 6 closed-composite segments of 1000 mm width each, including two key segments (F denotes crown segment and D denotes bottom segment), two left-hand segments (segment LU for upper one, while LD for lower one), and two right-hand segments (RU, RD represent upper and lower segments, respectively). The lining structure is symmetric along vertical and horizontal directions through the central point. Thus, both segment F and D share the same arc radius of 44450 mm, and for any standard segment (RU, RD and LU, LD), the arc radius measured is 1175 mm when connected to the key segments and 7837.5 mm when it is adjacent to other standard segments. The concrete grade of the segments is C55 with the compressive strength of

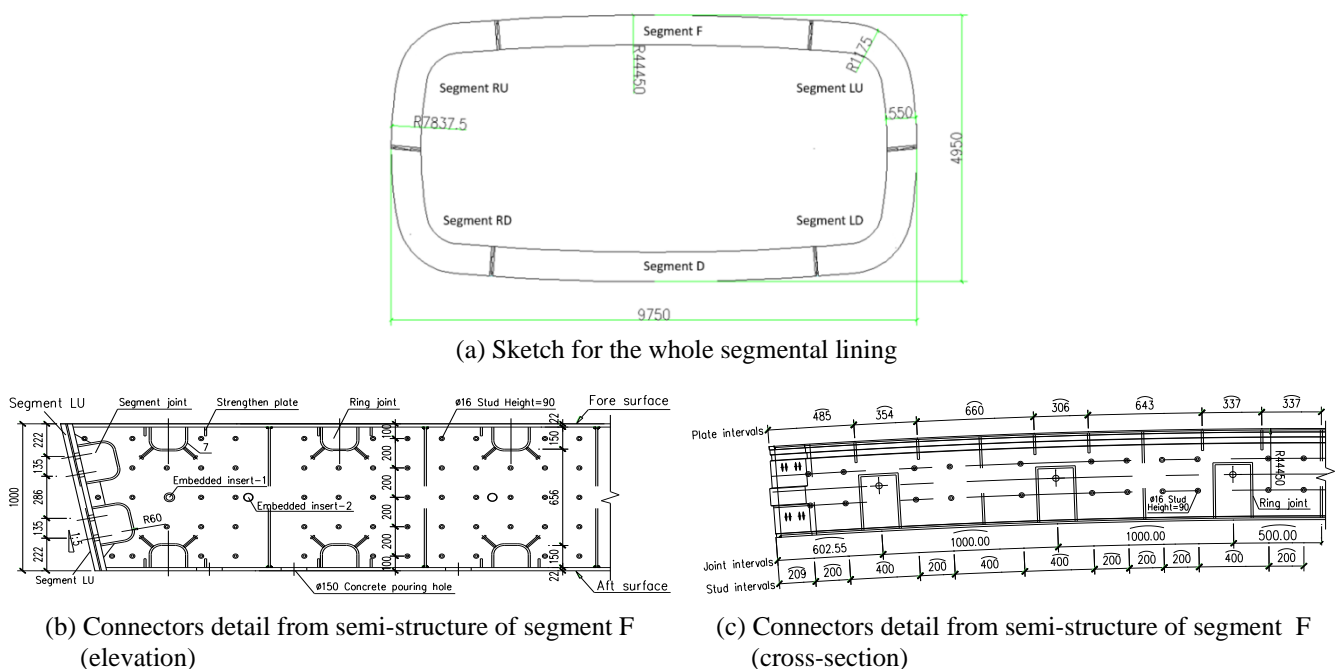
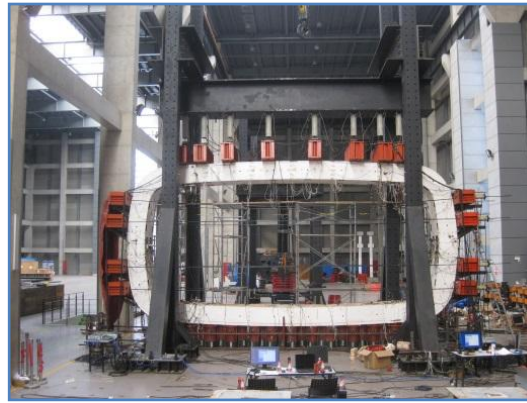


Fig. 1 The diagram for rectangular lining structure



(a) Overview of the tested lining

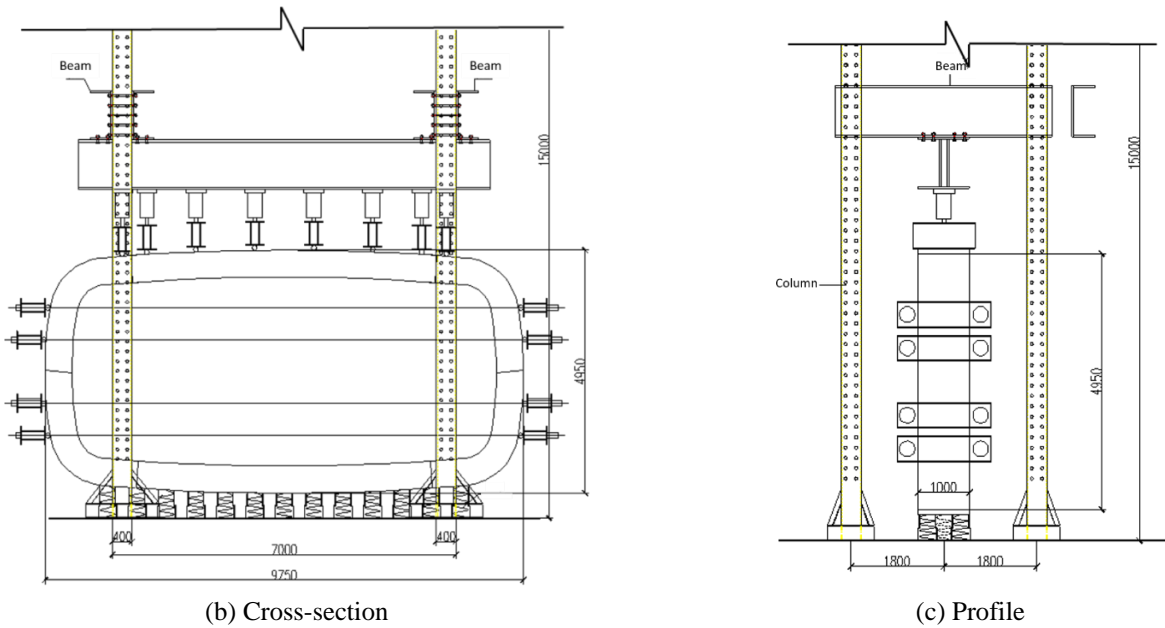


Fig. 2 The diagram for vertical loading system

35.3 MPa. The yield limit and the ultimate strength of the steel bar HRB335 are 335 MPa and 455 MPa, respectively. The diameters of bolts that connect the segments are 30 mm with the yield limit and ultimate strength of 400 MPa and 500 MPa, respectively. Each joint has 8 bolts.

2.2 Loading system

2.2.1 Vertical loading system

The vertical loading system which takes the self-weight effect into consideration was adopted in the test to simulate the influence of the pressure on the structure, shown in Figs.

2(a)-(c). The system was made up of a horizontal self-balance loading system and a vertical loading reaction frame. For the self-balance loading system, loads were applied on each point and its symmetric counterpart through two loading beams and two steel cables, i.e., jack exerted loads on load-bearing beam, which enabled a uniform distribution of the normal force, and then the force was transferred through cables to the other load-holding beam with anchor fastened. The loading reaction frame consisted of a main girder of 8.2 m in length and two counter force devices, each including two 15 m' height columns and a transverse beam with 8.2 m in length. Two ends of the

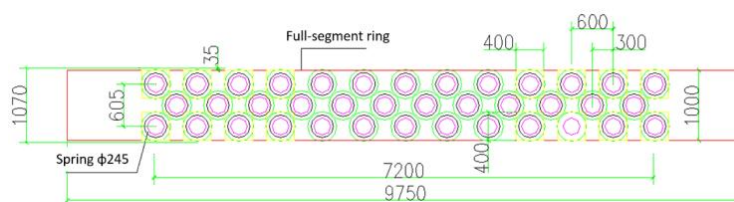


Fig. 3 The layout of the support springs



Fig. 4 The support spring for the test

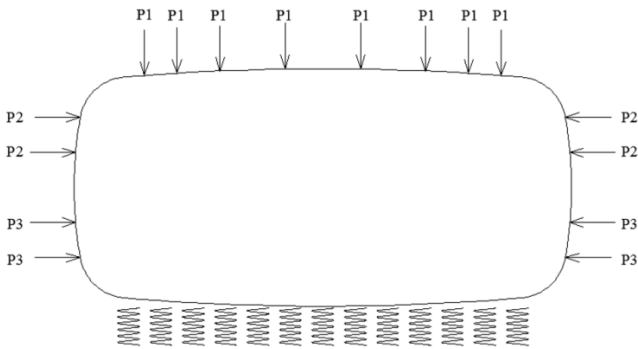


Fig. 5 Loads distribution in tests

transverse beam were connected with two columns by 10 bolts while two ends of the main girder were fastened to the transverse beam with 16 bolts. The size of the cross-section for each element is also illustrated in Fig. 2.

2.2.2 Support-spring system

The support-spring system was introduced in the test to simulate the soil effect in situ. As far as a full-segmental ring (1 m in longitudinal direction) was concerned, 38 springs were uniformly distributed along the width of the ring where they were regarded as contacting the ground closely, as shown in Fig. 3. Assume that the soil resistance coefficient  $K_s$  is  $5000 \text{ kN/m}^3$ , the total stiffness can then be calculated as  $7.6 \text{ m}^2 \times 5000 \text{ kN/m}^3 = 38000 \text{ kN/m}$ , which is equivalent to  $1000 \text{ kN/m}$  of elasticity coefficient for each spring. Fig. 4 shows one of the support springs used in the test, the outer diameter and the height were 245 mm and 670 mm, respectively.

2.3 Test procedure

The loading system was able to simulate different kinds of loads, such as strata resistance, soil and water pressure, as well as ground overload. The 16 load points were introduced to simulate the actual uniform-distributed loading condition, and were divided into 3 groups (see Fig. 5), i.e., 8 load points P1, 4 load points P2, and 4 load points P3. These experimental loads were based on the deformation and internal forces of the critical cross-section of an actual operating tunnel structure. Loads could be applied simultaneously at the load points.

The experiment was performed under load control and then under deformation control. The load was applied in a stepwise manner while corresponding data were collected within the individual time step. As the degree of nonlinearity of the load-deformation relationship increased, the load was further increased and data were continuously collected until the end of the experiment. By increasing the loads, the static loading process and, furthermore, the failure mechanism and the ultimate bearing capacity of the segmental lining strengthened by steel-plates were simulated. The loading process contained three stages, as illustrated in Fig. 6.

- (1) Firstly, P1, P2 and P3 were increased simultaneously until P1 amounted to its design load of 225 kN (the 10th loading step), at this time, the values of P2 and P3 were 75 kN and 94 kN, respectively.
- (2) Then loads were continuously increased in a stepwise manner until P2, P3 reached the values of their passive earth pressure, i.e., up to 125 kN, 158 kN (the 17th loading step), respectively. Meanwhile, the value for P1 was 350 kN (the coefficient of lateral earth pressure was 0.6). In the first two stages, load control was used.
- (3) P2, P3 were kept constant while P1 was further increased until the ultimate bearing capacity was reached, i.e., up to 540 kN. In this stage, displacement control was used.

After P1 reaching its maximum value of 540 kN, P1, P2 and P3 were unloaded simultaneously in steps of a

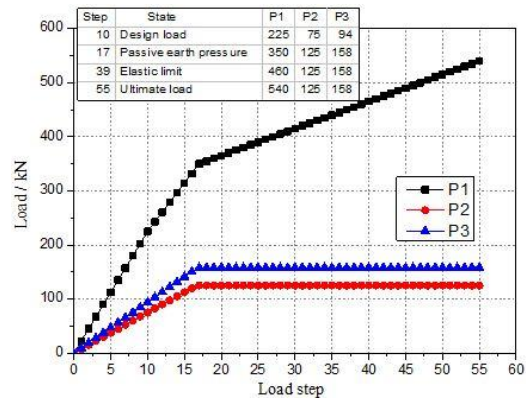


Fig. 6 Load levels versus load steps for loading process

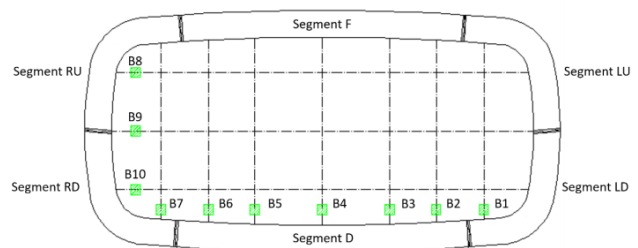


Fig. 7 The distribution of sensors for the displacement of the whole ring structure

gradually decreased scale from their maximum value, i.e., from 0.9, 0.8, 0.7,....., 0.1, to 0.

### 3. Experimental results

The data measured and collected in the framework to investigate the failure mechanism and the ultimate bearing capacity of the strengthened segmental lining were then presented, including the displacements and the internal forces of the entire structure, and the stain and stress of the bolts at each joints.

#### 3.1 Structural deformation

The overall deformation of the cross-section was measured by a line-displacement meter LVDT (Linear Variable Differential Transformer). The measurement system contained 10 displacement sensors, 7 in vertical direction and 3 in horizontal direction, all of which were fixed at inner lining to the steel plate, distributed along the cross-section, as shown in Fig. 7. By measuring the relative distance variation of each line that links with sensor, the corresponding convergences were obtained.

##### 3.1.1 Structural vertical deformation

For each vertical measurement points (B1~B7, shown in

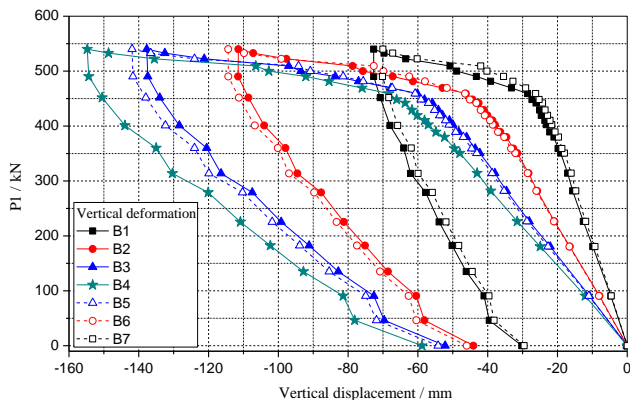


Fig. 8 Measurements of vertical deformation from sensors B1-B7

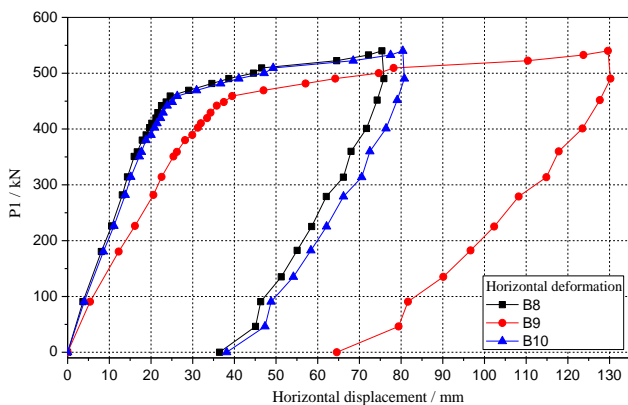


Fig. 9 Measurements of horizontal deformation from sensors B8-B10

Fig. 7), the development of structural vertical deformation under the variation of load P1 can be measured by the corresponding sensors, as clarified in Fig. 8, where negative values indicate the decrease of the relative distance.

With the load P1 gradually increased to its maximum value, the whole structure experienced two distinct types of deformation in the form of compression. At the first, the elastic stage, the deformation linearly increased to reach its elastic limit, which is corresponding to the load 460 kN, the 39th loading step of P1. Of all the values, the highest value occurs at the middle sensor B4 with the value of -68.33 mm. Then in yield stage, the deformation accumulated even more rapidly, much faster than the increment of the load until reaching its ultimate value of 540 kN (the 55th loading step). At this point, the vertical displacement from any of the sensors reached its maximum value. For example, sensor B4 showed that the maximum vertical displacement was -154.76 mm, which was equivalent to 3.13% of the total structural width. As the load P1 reduced from its maximum value to zero, all of the values from 7 sensors demonstrated linear regression trend with residual deformation ranging from -30 mm to -60 mm, whereas with different gradients, for example, at the point of P1 unloading to 450 kN (83% of the ultimate load), the highest deformation at the middle sensor B4 was -150.48, which was equivalent to approximately 2.2 times of the lowest values measured in sensor B1 or B7.

##### 3.1.2 Structural horizontal deformation

There were three sensors (B8~B10) that measure the structural horizontal displacement, as shown in Fig. 9, whereby the positive values indicate the increase of the relative distance.

The horizontal deformation presented an outward feature, whereas the mode of the displacement development was almost the same as that of the vertical displacement development: with the load added, the deformation gradually accumulated until the load reached the elastic limit ( $P1 = 460$  kN), and then showed a rapid increase to its maximum value. For example, the largest displacement occurred at the middle sensor B9 was 129.61 mm ( $P1 = 540$  kN), which accounted for 2.62% of the total structural height; during the unloading period, residual deformation was also left when the load reduced to zero ranging from 36 mm to 65 mm, a little larger than those existed in vertical deformation.

#### 3.2 Segmental strains of key sections

Segmental stains were measured by strain gauges deployed at the key sections of the steel plates. Twenty-two key sections were selected, each of which includes two pairs of sections, i.e., inner and outer surfaces, as well as fore and aft surfaces. Thus, 111 strain gauges were elaborately arranged along these inner-and-outer surfaces of all 22 key sections. For any section of each inner or outer surface, three measurement points were deployed along 1000 mm's longitudinal length at the equal interval, except for the bottom five key sections (No. 10-No. 14). Due to the existence of the support-spring system, strain gauges were only installed along the inner surface on three key sections

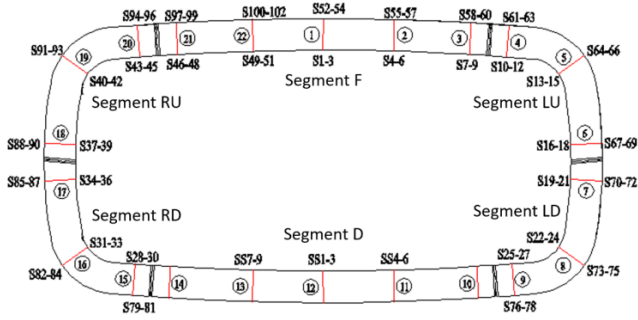


Fig. 10 The distribution of strain gauges on both inner and outer surfaces

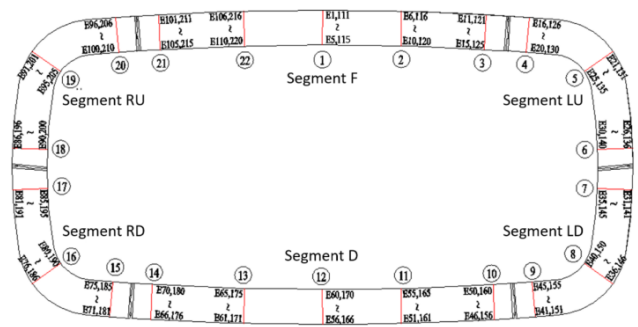


Fig. 11 The distribution of strain gauges on both aft and fore surfaces

(No. 11-No. 13), as shown in Fig. 10.

It is well known that for rectangular lining structure the maximum bending moments develop at the crown and the waist, therefore, the NO. 1 and NO. 17(or NO. 18) sections were firstly selected to investigate the corresponding strain variation in detail.

**3.2.1 The strain on the fore and aft surfaces**  
**NO. 1 section**

For No. 1 section, strain gauges distributed along the aft and fore surfaces were E1-E5 and E111-E115, respectively, as illustrated in Fig. 11. Noticeably, the strain gauges were numbered beginning with the outer edge. As P1 step wisely increased to its ultimate value and finally unloaded to zero,

the strain variation along aft and fore surfaces of No.1 section were shown in Figs. 12(a)-(b), respectively. The positive and negative strain signified the behavior of the segment when was in tension and compression, respectively.

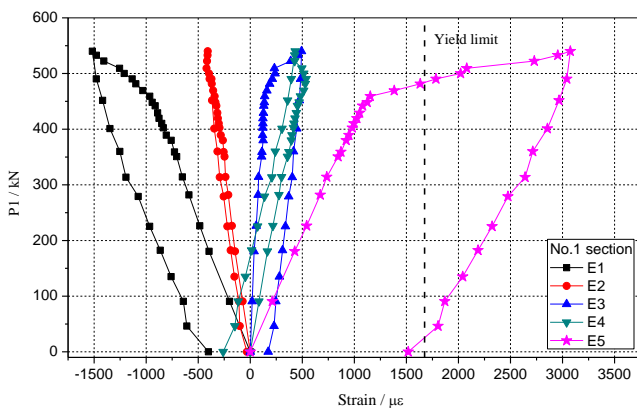
Due to the symmetric distribution of the loading system along the profile, the P1-strain curves, for both the aft surface and the fore surface, were almost the same, which in turn reflected the fact that the results of the experiment were reliable and reasonable. With P1 gradually added, the strain increased with the following characteristics:

- (1) Above the neutral plane (outer edge of 550 mm' thickness), the values of strain E1-E2 (or E111-E112) were negative, and decreased when approaching the neutral plane;
- (2) Below the neutral plane, the value of strain E4-E5 (or E114-E115) were positive, and increased when getting close to the inner edge, for example, as load P1 reaching the value of 490 kN (the 45th loading step), the strains of E5 accumulated to 1784  $\mu\epsilon$ ; moreover, at the point of P1 reaching its ultimate value (P1 = 540 kN), the strains of E5 or E115 culminated with the values of 3074.42  $\mu\epsilon$  and 3610.99  $\mu\epsilon$ , respectively, far beyond the steel bearing capacity of the yield limit of 1675  $\mu\epsilon$ . Noticeably, it is at this inner edge that the segment was subjected to the maximum positive bending moment under the vertical loading condition.
- (3) Finally, the strain from E3 and E113 were so close to zero because of the fact that they were both installed on the neutral plane.

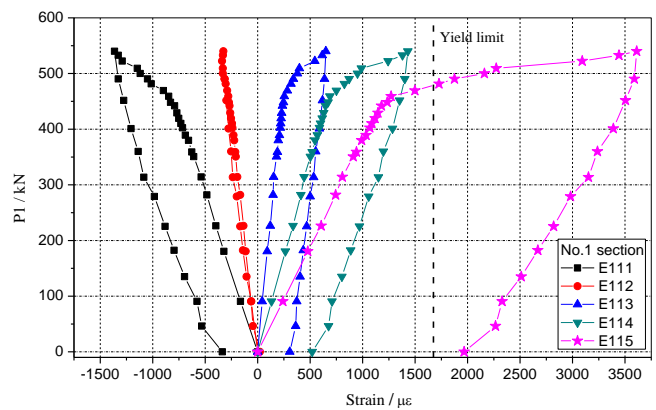
During the unloading period, the values of strain reduced. However, substantial residual strain remained as the load reduced to zero, especially at lower surface, where the part of structure experienced plastic deformation after the elastic deformation stage. The maximum residual strain occurred at E115 (or E5) with the value of 1966.86  $\mu\epsilon$  (or 1517.3  $\mu\epsilon$ ).

**NO. 17 section**

For NO.17 section, strain gauges installed along the aft and fore surfaces were E81-E85 and E191-E195, respec-



(a) Aft surface



(b) Fore surface

Fig. 12 P1 versus strain curves on No. 1 section

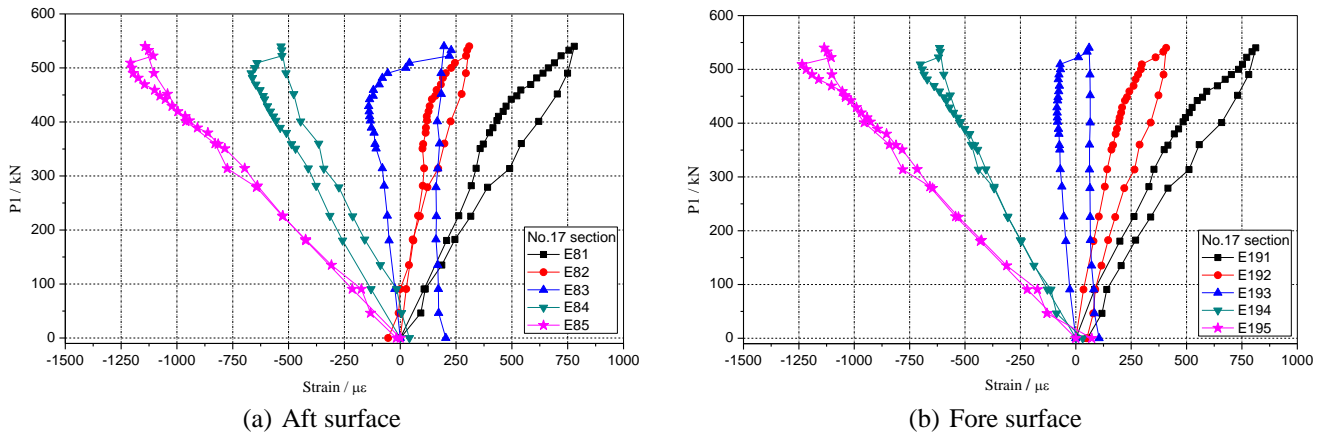


Fig. 13 P1 versus strain curves on No. 17 section

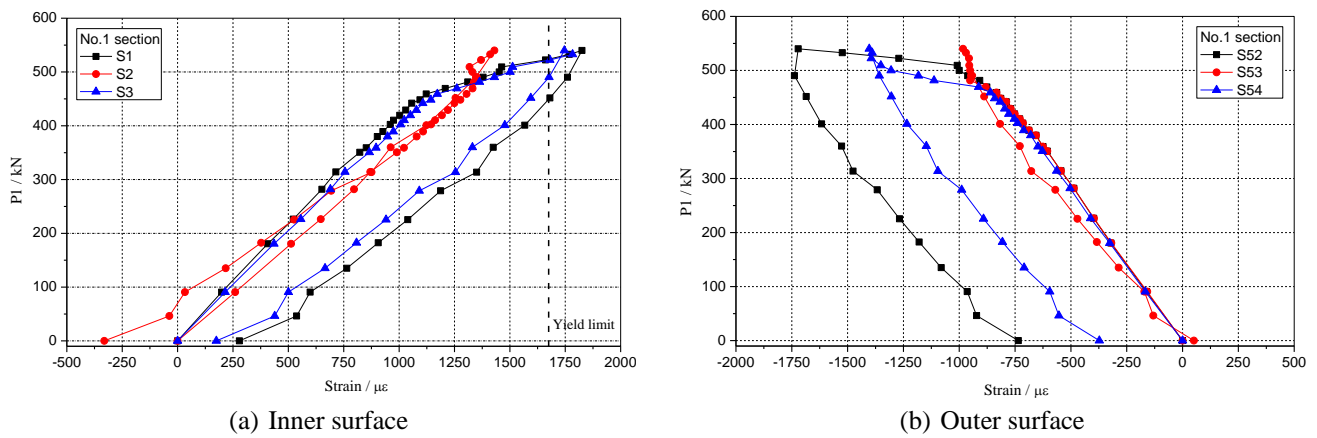


Fig. 14 P1 versus strain curves on No. 1 section

tively, as illustrated in Fig. 11. As P1 gradually increased to its ultimate value and then completely unloaded, the strain variation along aft and fore surfaces of No. 17 section are shown in Figs. 13(a)-(b), respectively.

The stains increased with P1 gradually added, moreover, negative strains were a little larger than that of the positive values, but both occurred and increased when approaching further to the edges of the lining, where the maximum bending moment developed. For example, at the point of P1 reaching its ultimate value ( $P1 = 540 \text{ kN}$ ), the maximum strain occurred at the E85 (or E195), with the values of  $-1042 \mu\epsilon$  and  $-1041 \mu\epsilon$ , respectively, leaving considerable margins to the bearing capacity of the steel plate. Likewise, there was almost no strain existed at the middle part of E3 or E113. In addition, as the load decreased to zero, the residual strain left was negligible; for example, the residual strain measured from E82 was only  $-54\mu\epsilon$ , mainly the elastic deformation that had happened in this section.

### 3.2.2 The strain on the inner and outer surfaces NO. 1 section

For No. 1 section, strain gauges distributed along the outer and inner surfaces were S52-S54 and S1-S3, respectively, as illustrated in Fig. 10. Noticeably, the strain gauges were numbered beginning from the aft surface side. As P1 stepwisely increased to its ultimate value and then

unloaded to zero, the strain variation along the inner and outer surfaces of No. 1 section are shown in Figs. 14(a)-(b), respectively.

No. 1 section was in the middle of crown segment. From the mechanical behavior of this structure, it is well known that under the vertical loads, the inner surface would be subjected to tensile stress while the outer surface would be in compression, which was consistent with the measurement results with inner and outer surfaces showing positive and negative values. Besides, the values of strain from inner surface were slightly larger than that of the absolute values from outer surface, for example, when P1 reached 522 kN (the 51st loading step), the stain of S3 from inner surface increased to  $1680.82 \mu\epsilon$ , just beyond the yield strain ( $\epsilon_y = 1675 \mu\epsilon$ ), resulting the steel plate yielded; while for the same load, the outer counterpart was still within the bearing capacity. Moreover, the maximum strain under the maximum load ( $P1 = 540 \text{ kN}$ , the 55th loading step) for inner and out surfaces were  $1825.33 \mu\epsilon$  and  $-1721 \mu\epsilon$ , respectively. However, both the inner or outer curves shared similarities: with P1 gradually increased, the deformation accumulated, and the strain at the sides developed much faster than the strain of the central one; when P1 reached 540 kN, both strains had shown that the steel plate yielded in individual subdomains. Finally, as the load decreased to zero, substantial residual strain remained, that was because

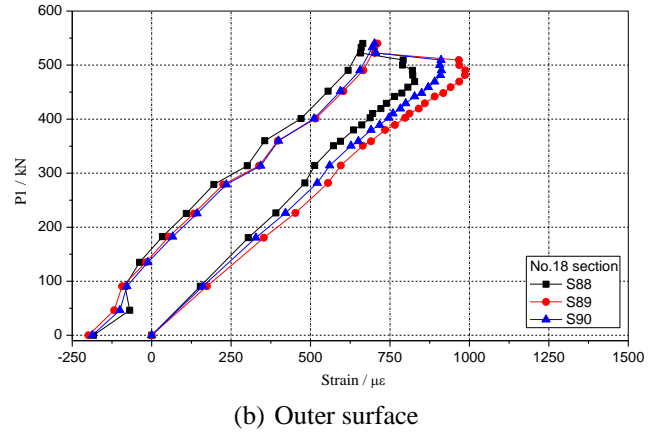
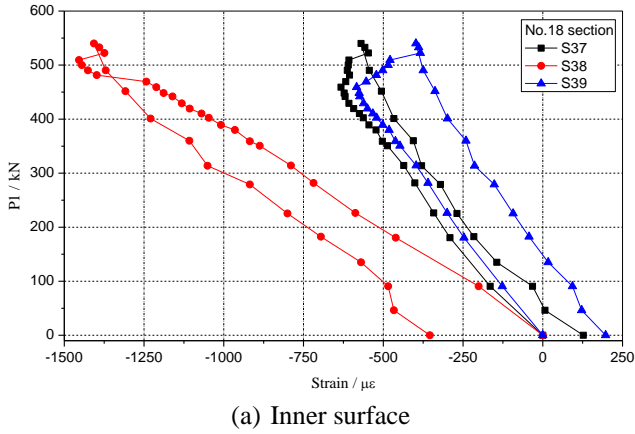


Fig. 15 P1 versus strain curves on No. 18 section

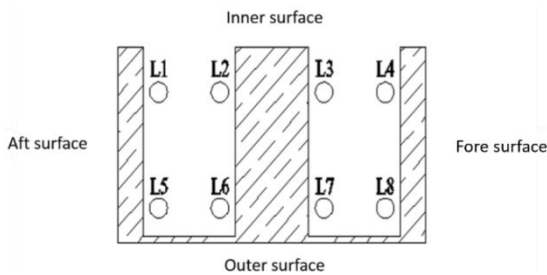


Fig. 16 The distribution of bolts in each segmental joint

of not only elastic deformation, but also plastic deformation subsequently generated from the steel plate in this region.

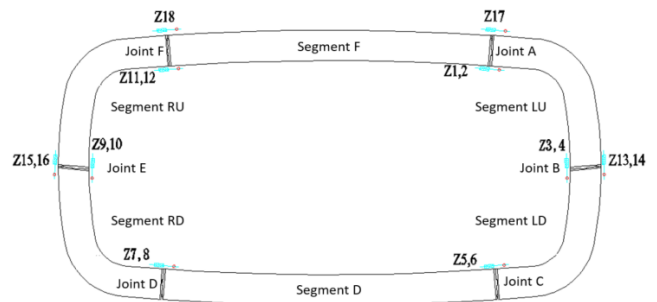
**NO. 18 section**

For No. 18 section, strain gauges distributed along the outer and inner surfaces were S88-S90 and S37-S39, respectively, as illustrated in Fig. 10. As P1 step wisely added to its ultimate value and then completely unload, the strain variations along the inner and outer surfaces of No.18 section are shown in Figs. 15(a)-(b), respectively.

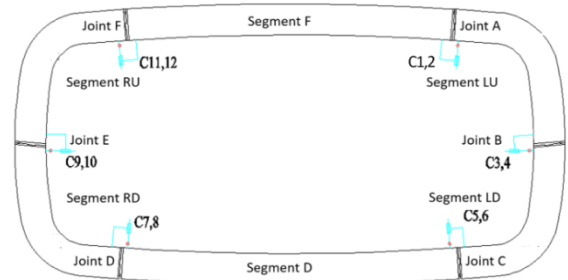
No. 18 section existed in the waist position of the lining structure, contrary to No. 1 section in the crown, the outer surface was in tension while the inner surface was subjected to compressive stress under the vertical loads. In general, as the load P1 gradually added, the variation of strains developed in the outer surface were larger than that occurred in the inner surface; as the load decreased to zero, the strains reduced but certain residual strains remained. It is worth noting that the maximum strains did not correspond to the ultimate load, for example, when the load P1 added to 490 kN, S89 from outer surface on No. 18 section topped at the value of 987.0  $\mu\epsilon$ , and then decreased to 710.5  $\mu\epsilon$  under the ultimate load of 540 kN. It indicated that the waist segments had modified deformation to suit the plastic state of the whole structure.

**3.3 Segmental joints and bolts**

There were 6 segmental joints around the whole lining structure (A~F, see Figs. 17(a)-(b)), and each joint was connected by 8 bolts (No. L1~L8), numbered from inner to outer surface, and then from aft to fore surface, as shown in



(a) Opening measurement points



(b) Stepped measurement points

Fig. 17 The distribution of measurement points in each segmental joint

Fig. 16. In respect of each segmental joint, along 1000 mm's longitudinal length (i.e., the width of each segment), inductive displacement transducers were fixed to measure the corresponding displacement under each load step, including 2 stepped measurement points and 2 opening measurement points, which were installed on the inner surface; besides, for each B and E segmental joints, 2 opening measurement points were fixed on the outer surface, as well as for each A and F segmental joints, 1 opening measurement point was fixed on the outer surface, as illustrated in Figs. 17(a)-(b). Noticeably, values from stepped measurement points were the relative displacement of two adjacent segments along the radial direction; while values from opening measurement points represented the relative displacement of two adjacent segments along the circumferential direction.

As far as the symmetrical loading condition is concerned,

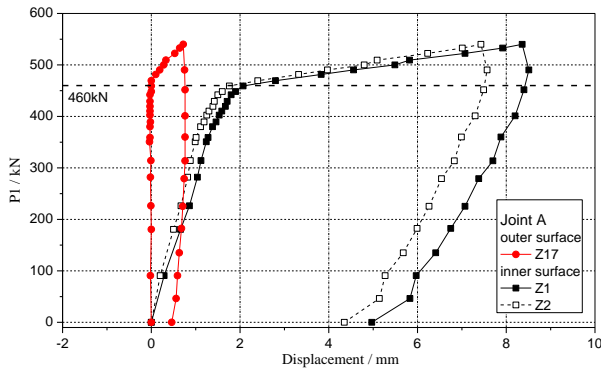


Fig. 18 P1 versus opening displacement curve for joint A

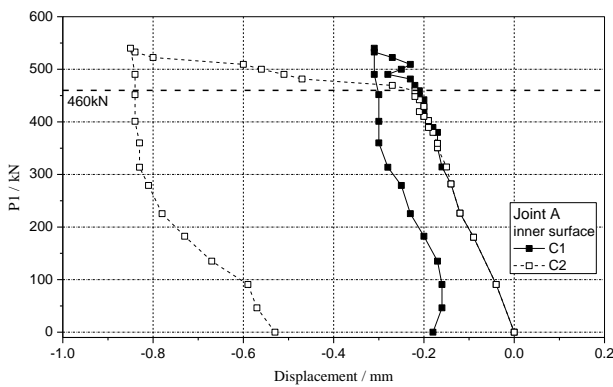


Fig. 19 P1 versus stepped displacement curves on inner surface for joint A

only half segmental joints and bolts referring to the middle vertical axial are discussed here, because of the fact that each joint and its symmetrical counterpart have similar results. Nevertheless, better data can be chosen for analysis in case of values staggering.

### 3.3.1 Joint A (or joint F)

Measurement points for joint A consisted of 2 opening points (No. Z1, Z2) and 2 stepped points (No. C1, C2) along the inner surface, also 1 opening point (No. Z17) on the outer surface. Joint F, existing between segment F and RU, was connected by 8 bolts, numbered FL1~FL8. 2 strain measurement points were installed on each bolt, while one axial force gauge was installed on FL2.

#### Joint opening displacement

For joint A, the values from opening measurement points on the inner and outer surface are shown in Fig. 18.

While for the inner surface, during the early stage of the loading period, the joint remained almost unchanged. When P1 reached about 460 kN, the relative displacement became apparent, and increased substantially to the maximum displacement of 8.36 mm at the load P1 of 540 kN. As the load decreased, the relative displacement reduced, but the residual displacement was left with the maximum value of 4.97 mm. However, the opening did not extend further, for the load-unload circle, the outer surface of joint A remained almost unchanged.

#### Joint stepped displacement

For joint A, the values from stepped measurement points on inner surface are shown in Fig. 19.

The absolute values of stepped displacements were much less than the opening values. The joint had remained almost unchanged until P1 reached certain value, and then the stepped displacement became apparent with the maximum value of -0.85 mm, where the negative signs meant segment F was relatively downward. As load P1 reduced to zero, slight residual displacement remained with the maximum value of -0.53 mm.

#### Bolt strain and axial force

For joint F, Fig. 20 shows the strains from 8 bolts FL1~FL8, and Fig. 21 illustrates the axial force from bolt FL2.

During the whole stage of the experiment, strain variation for bolts close to the inner surface (FL1~FL4) were far larger than that of bolts adjacent to the outer surface (FL5~FL8), which remained almost unchanged and the residual strains left were negligible. With respect to the bolts FL1~FL4, the strain variation had been limited until P1 reached certain value, and from there onwards, both strain and the axial force showed a significant and steady increase. When P1 added to 540 kN, the maximum strain occurred on bolt FL4 had the value of 4853  $\mu\epsilon$ , within its yield limit of 5059  $\mu\epsilon$ . As P1 reduced to zero, the residual

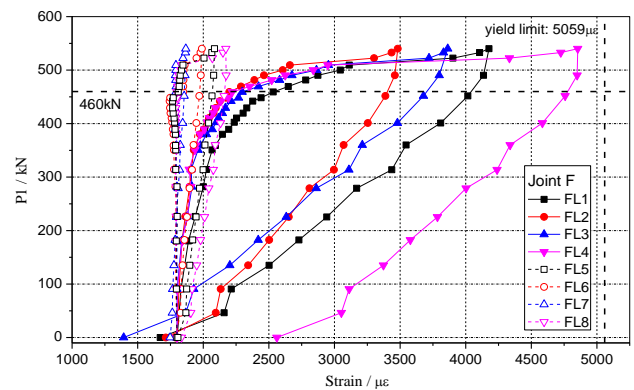


Fig. 20 P1 versus strain curves from bolts for joint F

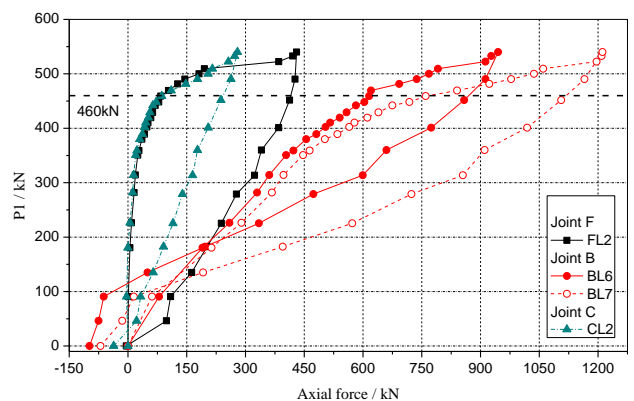


Fig. 21 P1 versus axial force curves from bolts for joint F, B and C

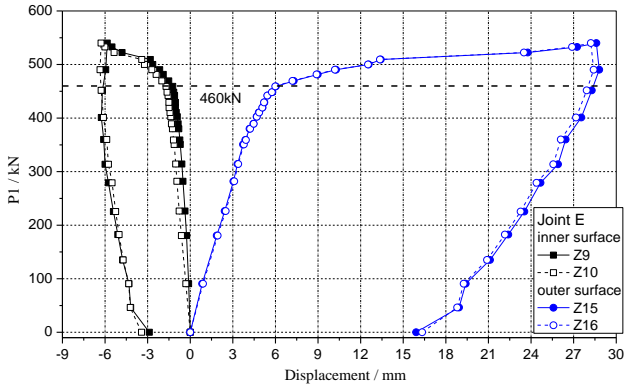


Fig. 22 P1 versus opening displacement curves for joint E

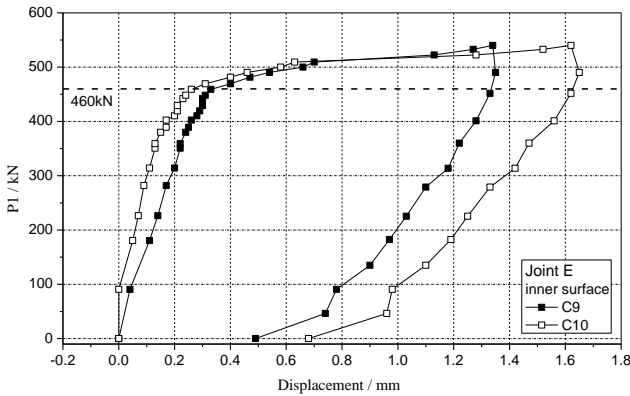


Fig. 23 P1 versus stepped displacement curves on inner surface for joint E

residual strain left with the maximum value was  $2560 \mu\epsilon$  on FL4.

**3.3.2 Joint B (or joint E)**

Measurement points for joint E consisted of 2 opening points (No. Z9, Z10) and 2 stepped points (No. C9, C10) along the inner surface, and 2 opening points (No. Z15, Z16) on the outer surface. Joint B, existing between segment LU and LD, was connected by 8 bolts, numbered BL1~BL8. 2 strain measurement points were installed on each bolt, while two axial force gauges were installed on BL6 and BL7.

Joint opening (compression) displacement

With respect to joint E, the values from opening measurement points on the inner and outer surface are shown in Fig. 22.

For the inner surface, during the early stage of the loading period, the joint remained almost unchanged. When P1 added about 460 kN, the deformation became apparent, and reached the ultimate value of -6.35 mm at the peak load, the negative sign of the displacement meant compression of the inner surface at that zone. As the load declined to zero, the maximum residual displacement was -3.43 mm. However, it works the other way around for the outer surface, the joint completely detached with the maximum opening value of 28.6 mm at the peak for P1, but residual opening of 16.33 mm was left when P1 was

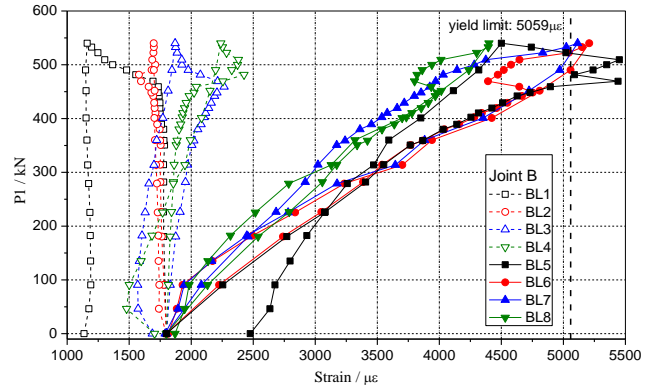


Fig. 24 P1 versus strain curves from bolts for joint B

completely unloaded.

Joint stepped displacement

With respect to joint E, the values from stepped measurement points on the inner surface are shown in Fig. 23.

Stepped displacement began to show a significant increase after P1 reached its elastic limit, and maximized at the ultimate P1 with the value of 1.62 mm, which meant the upper segment RD moved rightward relatively to its lower segment RD. As load P1 reduced to zero, considerable stepped displacement remained with the maximum value of 0.68 mm.

Bolt strain and axial force

With respect to joint B, Fig. 24 shows the strains from 8 bolts BL1~BL8, and Fig. 21 illustrates the axial forces from bolt BL6 and BL7.

During the whole stage of the experiment, strain variations for bolts close to the outer surface (BL5~BL8) were far larger than that of bolts adjacent to the inner surface (BL1~BL4). With respect to bolts BL5~BL8, as the load added, both strains and the corresponding axial forces showed an immediate and steady increase, and eventually nearly all these strains reached the yield limit of  $5059 \mu\epsilon$  in succession, for example, the corresponding loads for bolt BL5, BL6 and BL7 to yield were 470 kN, 533 kN and 540 kN, respectively. As P1 declined to zero, the residual strain left with the maximum value was  $2476 \mu\epsilon$  on BL5.

**3.3.3 Joint C**

Measurement points for joint C consisted of 2 opening points (No. Z5, Z6) and 2 stepped points (No. C5, C6) along the inner surface. Also Joint C, existing between segment LD and D, was connected by 8 bolts, numbered CL1~CL8. 2 strain measurement points were installed on each bolt, while one axial force gauge was installed on CL2.

Joint opening and stepped displacement

For joint C, the values from opening and stepped measurement points along the inner surface are shown in Fig. 25.

During the early stage of the loading period, the joint remained almost unchanged. When P1 reached about 460 kN, the opening displacement became apparent, and

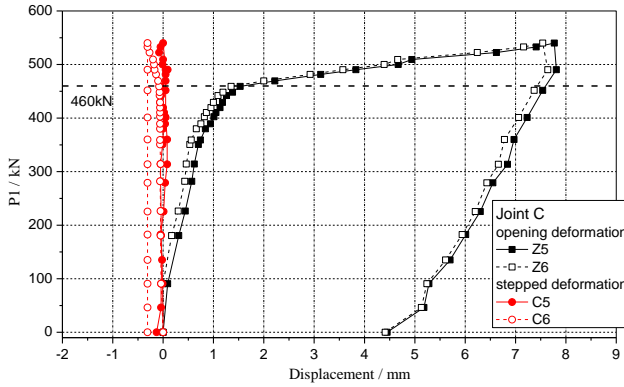


Fig. 25 P1 versus opening and stepped deformation on inner surface for joint C

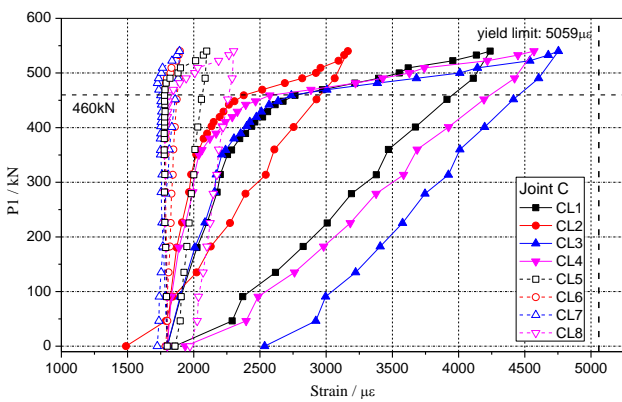


Fig. 26 P1 versus strain curves from bolts for joint C

reached the ultimate value of 7.77 mm at the ultimate load. As the load declined to zero, the maximum residual displacement was 4.45 mm.

The absolute values of stepped displacements were much less than the opening values. Also, just after P1 reached 460 kN, stepped displacement became apparent with the maximum value of -0.31 mm, where the negative sign of the displacement meant segment LD was relatively upward. As load P1 reduced to zero, residual stepped deformation still remained.

**Bolt strain and axial force**

For joint C, Fig. 26 shows the strains from 8 bolts CL1~CL8, also in Fig. 21, the axial force from bolt CL2 is illustrated.

During the whole stage of the experiment, strain variation for bolts close to the inner surface (CL1~CL4) were far larger than that of bolts adjacent to the outer surface (CL5~CL8), which remained almost unchanged and the residual strains left were negligible. With respect to the bolts CL1~CL4, the strain variation experienced a slight increase until P1 reached certain value, and from there onwards, both the strain and the axial force showed a remarkable and steady increase. When P1 was added to 540 kN, the maximum strain occurred on bolt CL3 had the value of 4753  $\mu\epsilon$ , within its yield limit of 5059  $\mu\epsilon$ . As P1 reduced to zero, residual strain remained and the maximum value was 2535  $\mu\epsilon$  on CL3.

**4. Discussion of results**

**4.1 Structural performance**

**4.1.1 Load – deformation relation**

Based on the structural deformation measured by 10 displacement sensors distributed along the cross-section (in Chapter 3.1), we can also obtain the variation of corresponding convergences along the segmental lining under the specific load. As the analysis aforementioned, the following loads were selected to further discuss the experiment (see Fig. 6): design load (P1 = 225 kN, the 10th loading step), elastic limit (P1 = 460 kN, the 39th loading step), ultimate load (P1 = 540 kN, the 55th loading step) and when unloaded to 85% of the ultimate load (P1 = 450 kN). The characteristics of the structural deformation under these loading loads are illustrated in Fig. 27.

Noticeably, the axial line is used to simply represent the lining structure, with the length and the height being 9200 mm and 4400 mm, respectively. And the figures here indicate the actual deformation, while the curves are formed from the data amplified 10 times for the sake of explicit expression and comparison. As shown in Fig. 27, in general, the maximum convergence and expansion occurred at crown and waist joints, respectively. Moreover, the conver-

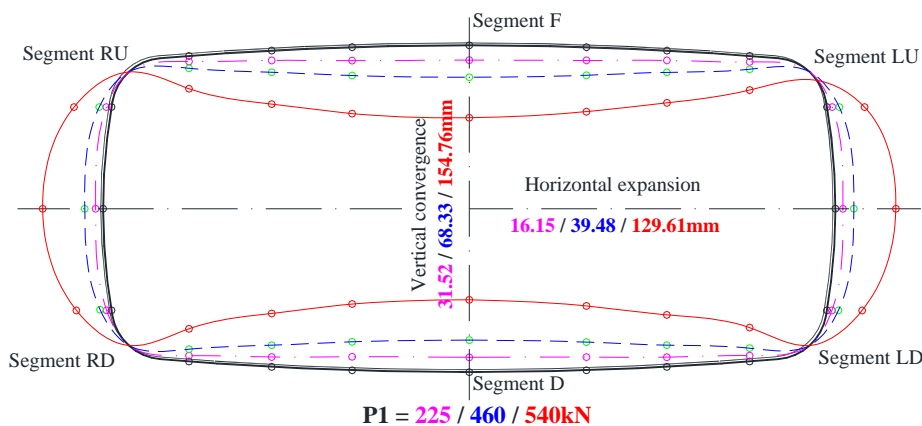


Fig. 27 Structural deformation under different loading condition (P1 = 225, 460, 540 kN)

gence was far larger than expansion, especially at the early stage of the loading, for example, under the design load, the largest decrease in vertical was 31.52 mm, which was 1.95 times of the largest horizontal increase with the value of 16.15 mm. However, deformation for the whole structure showed a kind of flattened trend as the load increased to its elastic limit, under which the ratio of maximum convergence to expansion was 1.73 and further reduced to 1.18 under the ultimate load. The trend indicates that the bearing capacity of the segmental lining was gradually provoked and propagated from crown to the waists, in accordance with the fact that when P1 unloaded to 450 kN, the residual deformation along the waists was significant (127.67 mm, 3.2 times of) compared with the expansion under previous elastic limit, while the residual deformation along the crown to bottom was 150.48 mm, 2.2 times of the convergence under elastic limit of 460 kN. However, the structural deformation under ultimate load of 540 kN and unload of 450 kN were almost the same, indicating that the ultimate load was far beyond the structure bearing capacity and substantial plastic deformation had happened.

4.1.2 Structural internal force

Through the segmental stains which were measured by strain gauges deployed on 22 key sections of the steel plates, the variation of the internal forces along the segmental lining under the specific load can then be produced. Likewise, three different loads as aforementioned,

design load, elastic limit and ultimate load were presented. Thus, the characteristics of the structural internal forces under these critical loads are illustrated in Figs. 28(a)-(b).

Noticeably, the positive bending moment denotes that the inner surface is in tension, which occurred around the crown and bottom part of the lining, while the negative bending moment signifies that the outer surface is in tension, which occurred along the two sides. Besides, the places for maximum positive and negative bending moment lied in the crown (or central bottom) and waist joints, respectively, exactly the same as that of the maximum convergence and expansion. Moreover, the maximum positive bending moment was far larger than the maximum negative bending moment. As the load added, the ratio of maximum positive bending moment to negative bending moment increased and even reached the maximum 2.1 under the ultimate load, which indicates that the top and bottom segments were more vulnerable and prone to losing the bearing capacity after exceeding the elastic limit. For example, the average strain in this part was about  $3300 \mu\epsilon$ , far beyond the steel yield strain,  $1675 \mu\epsilon$ , as shown in Figs. 12(a)-(b). With respect to axial forces, in general, the whole structure was subject to compression and the maximum axial forces happened around the waist joints.

4.1.3 Load – rotation relation of segmental joints

There are 6 segmental joints around the whole lining structure, and through the opening measurement points

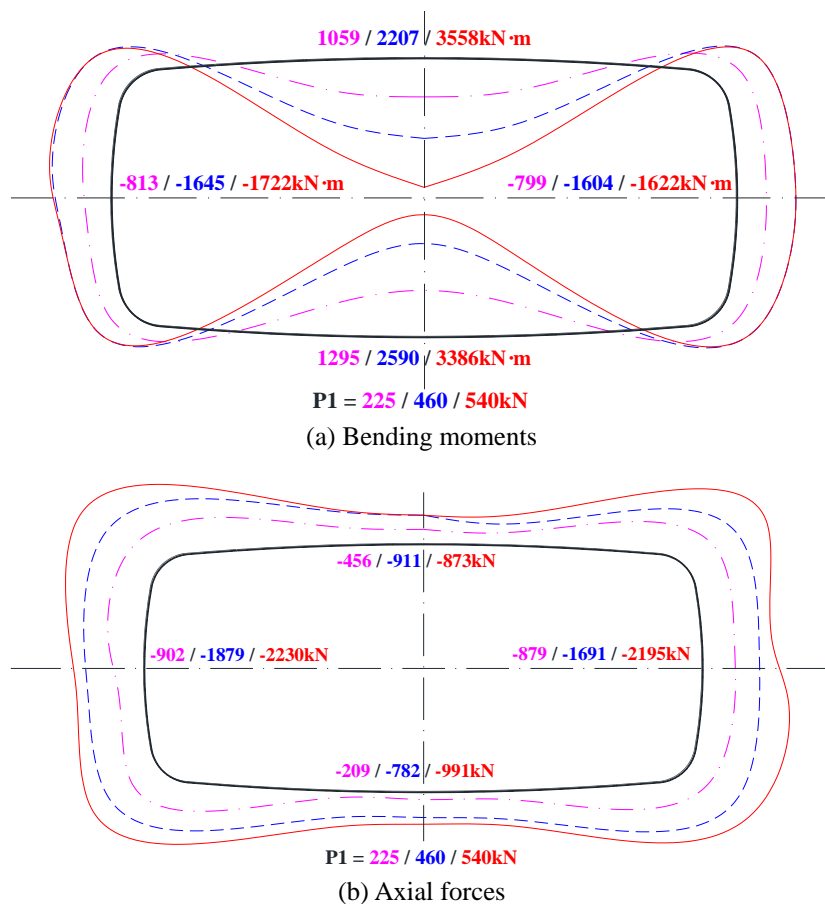


Fig. 28 Structural internal forces under different loading condition (P1 = 225, 460, 540 kN)

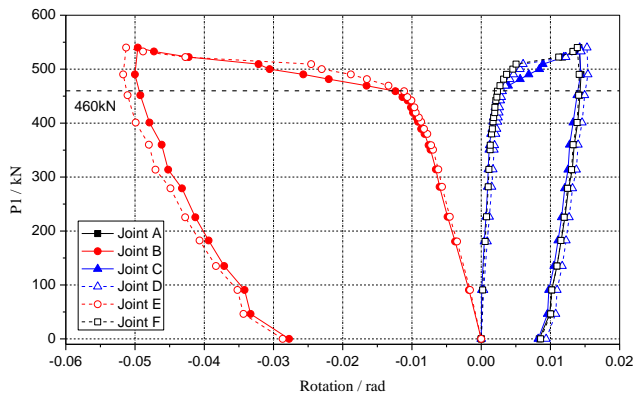


Fig. 29 Relation of rotation and loads for each joint

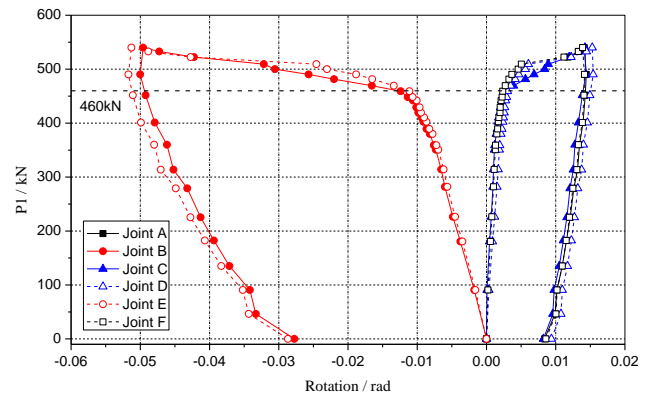


Fig. 30 Relation of average slip and loads for each joint

which were installed on the inner and outer surface at each joint (see Fig. 17(a)), the relation of joint rotation and load can then be calculated under the specific rotation center. Theoretically, the rotation center is at the bottom edge of the waterproof strip when the part is subjected to positive bending moment, while it lies in caulking as the part is subjected to negative bending moment. Furthermore, the actual rotation under each load is also taken into consideration and referenced. Therefore, the variation of the rotation for each joint under different loads are illustrated in Fig. 29, wherein positive rotation represents inner surface opening, and negative values signifies outer surface opening at each joint.

As load  $P_1$  gradually increased, the absolute rotation for each joint increased, and the opening values of outer surface at waist joints (B, E) were significant larger than the opening produced on the inner surface for the rest of the joints (A,C,D,F), which lie around the corners where the sign of the bending moment changed, from negative to positive and vice versa. The variation of the rotation curves indicated that the larger the bending moments, the higher the stiffness it needed to sustain the pressure acting on the lining structure. Whereas, once the loads increased and reached its yield strength, the structure would rapidly lose its bearing capacity and the residual rotation remained after the test.

#### 4.1.4 Load – slip relation of segmental joints

Through the stepped measurement points which were installed along the inner surface at each joint (see Fig. 17(b)), the relation of joint slip and load can then be calculated. Fig. 30 shows the variation of the slip for each joint under different loads, wherein the slip is the average and absolute value of the stepped displacement.

As load  $P_1$  gradually increased, the absolute slip for each joint increased, and just like the rotation variation at joints, the slip at waist joints (B,E) were far larger than the slip produced at the rest of the joints (A,C,D,F), for which the average slip is less than 0.6 mm. At the ultimate load, the maximum slip of joints B and E reached 1.6 mm and 1.5 mm, respectively, and considerable residual slip was left after the load was reduced to zero. However, there was no strong sign that the slip and its development were apparent from the observations after the test, and the development of

slip can even be controlled by the overlapping of tenon at joints.

## 4.2 Analysis of failure mechanism

### 4.2.1 Progressive structural failure Bolt yield at segmental joints

During the whole stage of the experiment, the bolts at joint A,C,D,F remained safe, especially for bolts adjacent to the outer surface (L5~L8), which were almost unchanged and the residual strains left were small. With respect to bolts L1~L4 on the other side, the strains changed rapidly when  $P_1$  reached elastic limit, the corresponding opening, however, was still far smaller than the waterproof limit 6 mm. At the ultimate load, the opening slightly exceeded the waterproof limit and the strains reached its maximum value too, but all were still within its yield limit of  $5059 \mu\epsilon$ ; as  $P_1$  reduced to zero, both residual strain and opening was left.

Somewhat different for bolts at joint B,E, during the whole stage of the experiment, strain variations for bolts close to the outer surface (L5~L8) were far larger than that of bolts adjacent to the inner surface (L1~L4), of which the strains were almost unchanged and the residual strains left were small. The opening, however, remained at the end of the test, but was still within the waterproof limit 6 mm. With respect to bolts L5~L8, the strains and opening increased rapidly when  $P_1$  reached elastic limit, and exceeded the yield limit and waterproof limit in succession before  $P_1$  reached the ultimate load; as  $P_1$  reduced to zero, both residual strain and opening were left. Thus, for joint B and E, respectively, as far as the yield limit ( $5059 \mu\epsilon$ ) and waterproof limit (6 mm) are concerned, certain parts which can be regarded as failure and its development are presented in Figs. 31(a)-(b) and Figs. 32(a)-(b). Nevertheless, the bolts after the tests were a testimony that no remarkable sliding or deformation had happened to them, see Figs. 33(a)-(b).

For all the segmental joints, the failure only happened at joint B and E, to be exactly, bolt L5~L8 (closed to the outer surface) yielded as load exceeded its bearing capacity and the opening of the outer surface increased to the extent that could affect its waterproof capacity. Thus, the development of the failure can be concluded as the following sequence. Firstly, when  $P_1$  was added to 460 kN, the opening reached

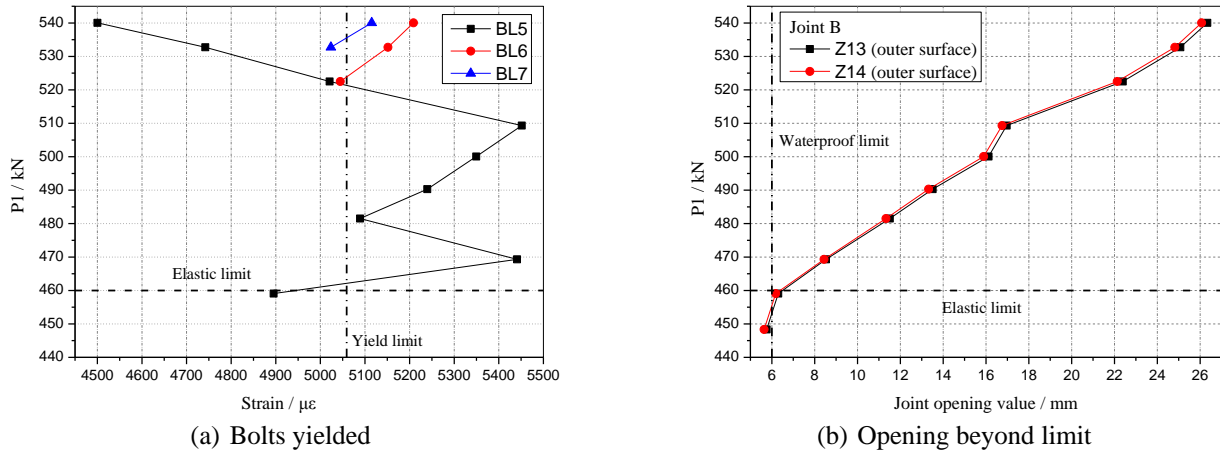


Fig. 31 Failure development at joint B

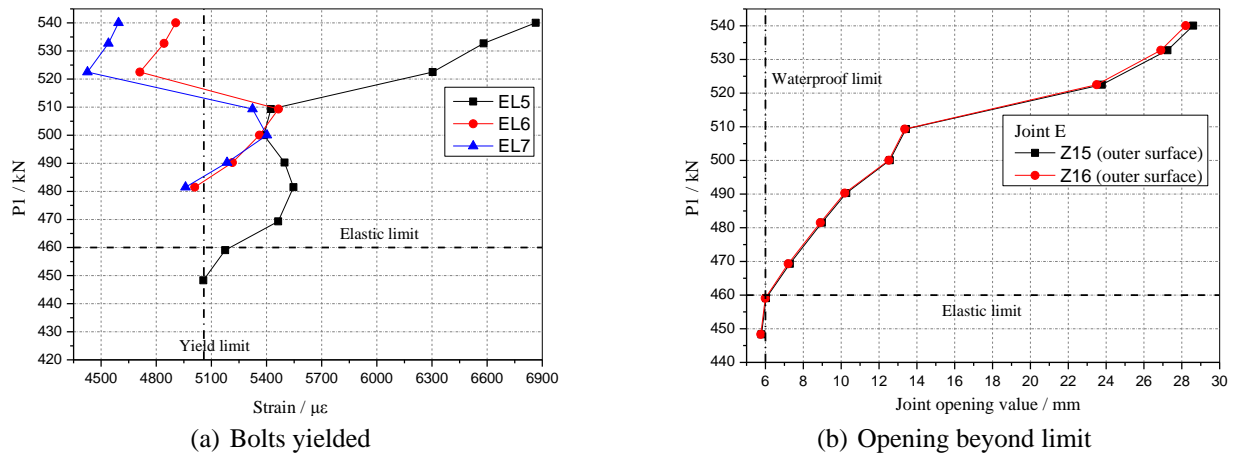


Fig. 32 Failure development at joint E



(a) Bolt BL5



(b) Bolt EL5

Fig. 33 Bolts after the tests

its waterproof limit at both joint E and joint B, and also bolt EL5 from joint E yielded; then bolt BL5 from joint B yielded when  $P_1$  reached about 470 kN; thereafter, bolt EL6 and bolt EL7 from joint E yielded as the load was further increased to 490 kN; finally, BL6 from joint B yielded under the load of 532 kN and consequently, BL7 from joint B yielded when the load reached ultimate level.

Steel plate yield at segments

Theoretically, the larger the internal forces (especially

bending moments), the higher the possibility that the corresponding steel plate may be subjected to yield. The data from the test results validated this with the fact that only steel plates from segment F and D, did the strain increase beyond the limit of the yield strength. Thus, as far as the strain yield limit ( $1675 \mu\epsilon$ ) of the steel plate is concerned, with respect to segment F and D, parts which can be regarded as failure and its development are shown in Figs. 34 and 35, respectively.

For all the measurement points from segment F to D

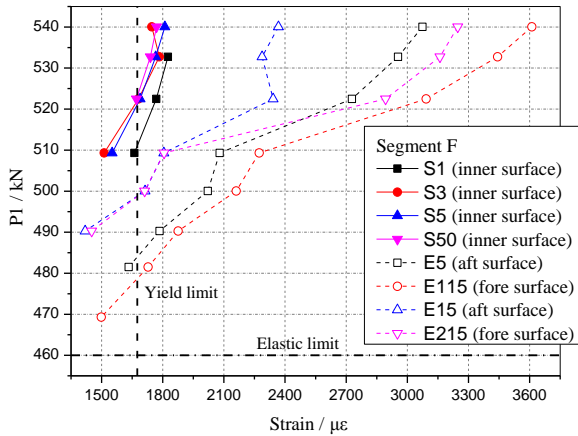


Fig. 34 Failure development at segment F

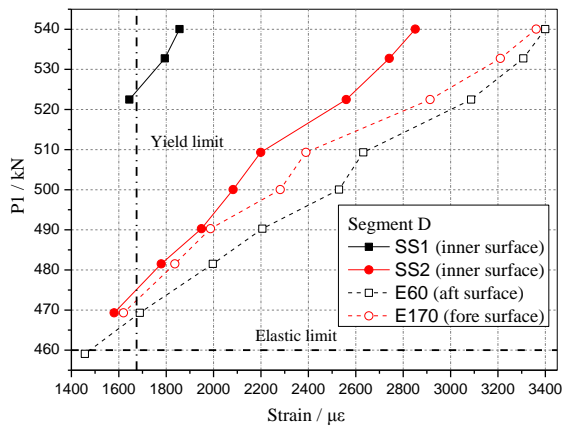


Fig. 35 Failure development at segment D

(see Figs. 10-11), the failure only happened at points shown in Figs. 34 and 35, to be exactly, the points yielded as their strains under certain load exceeded the strain yield limit, and consequently left considerable residual deformation when the load decreased to zero. Besides, it is along the inner surface or close to the inner surface (when along the aft or fore surface condition) that these points located, corresponding to locations where the maximum positive bending moments occurred. In general, the points along the aft or fore surface yielded prior to the points along the inner surface. For example, for segment D and F, respectively, their first points to yield happened at E60 and E115, under the load of 480 kN and 470 kN respectively; following that, E170 and E5 yielded as loads further increased to 480kN and 490 kN, respectively; thereafter, failure extended to the side points E215 and E15 of segment F under load 500 kN; finally, the points from inner surface began to yield, i.e., S1,S3 and the side points S5,S50 from segment F yielded simultaneously under load 520 kN, and consequently, SS1 from segment D yielded when the load reached 532kN, close to the ultimate load.

#### 4.2.2 Ultimate structural bearing capacity

In the test, either the opening beyond the waterproof limit or the strain exceeding the corresponding yield limit, can be considered as the ultimate bearing capacity of the

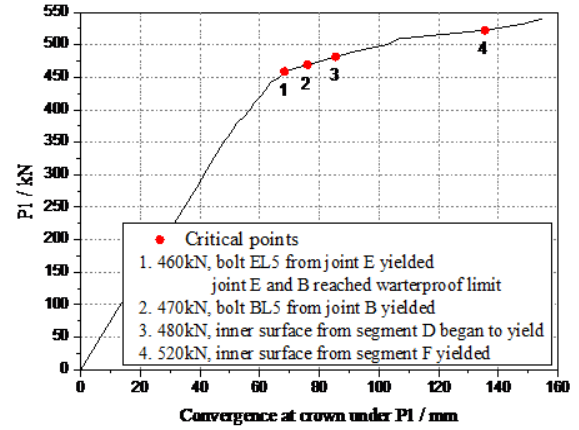


Fig. 36 The whole process of the structural failure development

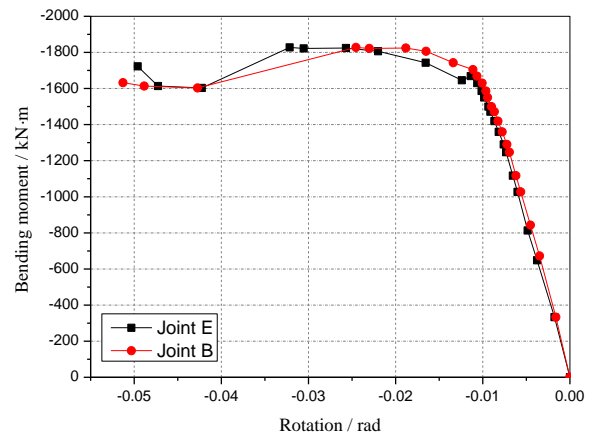


Fig. 37 The relation of rotation and bending moment at joint B and E

segmental lining structure. In the curve for load versus convergence at the crown (see Fig. 36), the progressive structural failure can be tracked by the critical points which indicated the bearing capacity of each component and also the ultimate structural deformation. For example, at the first stage (the load within the elastic limit 460 kN), the convergence linearly increased with the loads, and the tangent modulus of their relation represented the structural stiffness which remained the same and therefore guaranteed the structural deformation capacity; thereafter, with the first yield point happened, the stiffness began to reduce, and even faster as other failure points followed, as a result, the deformation increased substantially without limit until the test ended. Thus, it can be concluded that the improving of the structural stiffness by means of strengthening the segmental lining can increase the ultimate bearing capacity and reduce the deformation of the structure. Take joint B and E which yielded first for further analysis, as shown in Fig. 37 of the relation for rotation and bending moment, under the same bending moment, the rotation at joint B was slightly smaller than that of joint E, which signified that the ultimate bearing capacity at joint B was higher as a result of a larger stiffness to sustain the pressures acted on the segment.

## 5. Conclusions

The following conclusions are drawn from the experiment presented in this paper:

- For the rectangular segmental lining, the structural performance under loading can be summarized as follows:
  - (1) The maximum convergence and expansion occurred at the crown and waist, respectively. Moreover, the convergence was far larger than expansion.
  - (2) The positive bending moment occurred at the crown and bottom segments with the inner surfaces in tension; while the negative bending moment occurred along the two sides as the outer surface were subjected to tension. Furthermore, it was close to the four joints around the corners that the sign of the bending moment made a change. Moreover, the maximum positive bending moment was far larger than the maximum negative bending moment. The whole structure was subject to compression and the maximum axial forces happened around the waist joints.
  - (3) The maximum rotation happened at waist joint B and E with the opening developed at the outer surface; the maximum slip also occurred at joint B and E. As the load was reduced to zero, both residual rotation and slip was left.
- The segmental lining structure started to fail when bolts at waist joints yielded to the extent of the opening exceeding waterproof limit and the strain reached the yield limit. This led to a fast decrease of the stiffness of the whole structure and eventually a loss of the structural integrity as the inner surfaces along segment D and F yielded in succession and failed in function.
- The process of failure for bolts at both joints or steel plates share the same mode of three typical periods: at the early stage of the loading, the deformation was small and can be retrievable to zero as the loads withdraw; When load reached its elastic limit, the deformation became apparent and increased rapidly to the maximum value; As load unloaded to zero, residual deformation was left.
- From the curves of the failure development, considerable deformation remained which indicated that yield deformation happened besides elastic deformation, but as for the composite structure, the deformation characteristics, especially the state of its yield phase was not as typical or apparent as normal steel or concrete structure, but had the features of both.

The experimental data provide a basis for further investigation. Currently, a comprehensive numerical modeling approach is developed for the investigation of the nonlinear response of the composite lining structure. It will be used in further research concerning different failure

modes and the influence of various design parameters on the strength and the serviceability of rectangular segmental tunnel linings reinforced by steel plates.

## Acknowledgments

The research was financially supported by the National Natural Science Foundation of China (Grant No. 51578409) and the State Key Laboratory for Hazard Reduction in Civil Engineering, Tongji University (Grant No. SLDRCE14-B-27). Also, support by the NNSF(Grant No. 51108268) is gratefully acknowledged.

## References

- Bowerman, H., Coyle, N. and Chapman, J.C. (2002), "An innovative steel/concrete construction system", *Struct. Engr.*, **80**(20), 33-38.
- Clubley, S.K., Moy, S.S. and Xiao, R.Y. (2003), "Shear strength of steel-concrete-steel composite panels", *J. Constr. Steel Res.*, **59**(6), 795-808.
- Dai, X.X. and Liew, J.R. (2010), "Fatigue performance of lightweight steel-concrete-steel sandwich systems", *J. Constr. Steel Res.*, **66**(2), 256-276.
- Johnson, A.F. and David, M. (2010), "Failure mechanisms in energy-absorbing composite structures", *Philosoph. Magaz.*, **90**(31-32), 4245-4261.
- Leveque, D., Lauri, F., Mavel, A. and Carrere, N. (2013), "Investigation on failure mechanisms of composite structures subjected to 3D state of stresses", *Conference Proceedings of the Society for Experimental Mechanics Series*, New York, NY, USA, June.
- Liang, Q.Q., Uy, B. and Wright, H.D. (2004), "Local buckling of steel plates in double skin composite panels under biaxial compression and shear", *J. Struct. Eng.*, **130**(3), 443-451.
- Liew, J.R., Soheli, K. and Koh, C.G. (2009), "Impact tests on steel-concrete-steel sandwich beams with lightweight concrete core", *Eng. Struct.*, **31**(9), 2045-2059.
- McKinley, B. and Boswell, L.F. (2002), "Behavior of double skin composite construction", *J. Constr. Steel Res.*, **58**(10), 1347-1359.
- Nakamura, H., Kubota, T. and Furukawa, M. (2003), "Unified construction of running track tunnel and crossover tunnel for subway by rectangular shape double track cross-section shield machine", *Tunn. Undergr. Space Technol.*, **18**(2), 253-262.
- Subedi, N.K. and Coyle, N.R. (2002), "Improving the strength of fully composite steel-concrete-steel beam elements by increased surface roughness-an experimental study", *Eng. Struct.*, **24**(10), 1349-1355.
- Tian, C.Y., Xiao, C.Z., Chen, T. and Fu, X.Y. (2014), "Experimental study on through-beam connection system for concrete filled steel tube column-RC beam", *Steel Compos. Struct., Int. J.*, **16**(2), 187-201.
- Tomlinson, M., Tomlinson, A. and Chapman, M. (1989), "Shell composite construction for shallow draft immersed tube tunnels", *Proceedings of ICE International Conference on Immersed Tunnel Techniques*, Manchester, UK, April.
- Xie, M., Foundoukos, N. and Chapman, J.C. (2007), "Static tests on steel-concrete-steel sandwich beams", *J. Constr. Steel Res.*, **63**(6), 735-750.
- Yang, Y., Yu, Y.L., Guo, Y.X., Roeder, C.W., Xue, Y.C. and Shao, Y.J. (2016), "Experimental study on shear performance of partially precast castellated steel reinforced concrete (CPSRC) beams", *Steel Compos. Struct., Int. J.*, **21**(2), 289-302.

- Zhang, W.J. (2009), "Study on mechanical behavior and design of composite segment for shield tunnel", Ph.D. Dissertation; Waseda University, Tokyo, Japan.
- Zou, G.P., Xia, P.X., Shen, X.H. and Wang, P. (2016), "Investigation on the failure mechanism of steel-concrete steel composite beam", *Steel Compos. Struct., Int. J.*, **21**(6), 1183-1191.

*BU*